PNAS RESEARCH ARTICLE | APPLIED PHYSICAL SCIENCES

Open millifluidics based on powder-encased channels

Xiaoguang Li[a,1], Xianglong Pang[a], Haohao Jiang[a], Mei Duan[a], Heng Liu[a], Zhujun Yang[a], Yuhang Xi[a], and Thomas P. Russell[b,c,d,e,1]

Edited by Anna Balazs, University of Pittsburgh, Pittsburgh; received February 24, 2023; accepted May 31, 2023

Millifluidics, the manipulation of liquid flow in millimeter-sized channels, has been a revolutionary concept in chemical processing and engineering. The solid channels that contain the liquids, though, are not flexible in their design and modification, and prevent contact with the external environment. All-liquid constructs, on the other hand, while flexible and open, are imbedded in a liquid environment. Here, we provide a route to circumvent these limitations by encasing the liquids in a hydrophobic powder in air that jams on the surface, containing and isolating flowing fluids, offering flexibility and adaptability in design, as manifest in the ability to reconfigure, graft, and segment the constructs. Along with the open nature of these powder-contained channels that allow arbitrary connections/disconnections and substance addition/extraction, numerous applications can be opened in the biological, chemical, and material arenas.

open millifluidics | flow manipulation | structured liquids | interfacial jamming

Significance

Fluidic channels that are fully open contain and allow the flow of liquids while maintaining ready interaction with the environment, unlike common closed channel constructs. Based on the successive joining of liquid marbles using a facile fusion strategy, powder particle-encased channels that are open to the environment and can be easily reconfigured, grafted, and segmented are produced. These afford high flexibility and versatility to the manipulation and design. By use of various hydrophobic particulates, on-demand material selection and function can be imparted to the constructs.

Microfluidic and nanofluidic devices have had a significant impact in the engineering and chemical communities, particularly when the amount of materials available for study is limited. The size of the channels restricts the passage of larger entities, e.g., embryos or tumor spheroids (1), while fluid viscosities and the clogging of channels can pose severe impediments in their use (2). These can be circumvented by use of millifluidics that provide larger working channels that benefit external designs for in situ monitoring and real-time feedback, both useful for materials optimization (3, 4). Channel innovation is crucial for fluidics at any scale. Typically, the channels are sealed by four solid walls, closed to the environment. Open-channel designs in microfluidics have progressed considerably, where the flowing liquid is partly or fully open to air or an immiscible liquid (5–9). The use of the term "open" arises from the external accessibility of the channels, which allows the introduction or removal of reactants and fluids by piercing the interface with a needle without deleteriously effecting the channel, thus offering exceptional flexibility. By combining the use of patterned substrates and nanoparticle surfactants assembled at the fluid–fluid interface, open microfluidics and millifluidics, with channel sizes ranging from microns to millimeter, have been realized and show dynamic stability, owing to the particle coverage (9). However, these millifluidic devices must be imbedded in a liquid environment, and the patterned architecture cannot be tailored once fabricated.

Here, we put forth a strategy to fabricate fully open millifluidic devices that function in an air environment with tailorable architectures using commercially available powder particles. Interfacial particle jamming or gelation comprises a rigid casing that locks a liquid droplet into a nonequilibrium shape (10–15). The particle shell is open to the environment allowing interactions with solids, other liquids, or gases (16, 17). Previous studies demonstrated that shaped liquids-in-air could be obtained using several special particle sources, including a superhydrophobic film comprised of nanoparticles with extremely weak cohesive forces (14–20), a bed of millimeter-sized sheets of polygonal shapes (21), and a powder that can form a hydrogel layer on a water surface (13). From the methods point of view, using a rolling process or a strong electric field-induced merging can readily bring about rod-shaped liquids, but with short lengths (13, 22). Despite the achievements, the available particle type, and the available size range, shape designability and controllability of the resulting liquid constructs are limited. It is still a significant challenge to generate channel-structured liquid constructs that are encased by common powders comprised of any hydrophobic particles with on-demand available shapes and sizes and without requiring extreme conditions or strenuous manipulations. Moreover, the generation and performance of liquid flow in a particle-encased channel, which is the base for fluidics applications, remains to be addressed. Here, we demonstrate a strategy to address these issues and realize fully open millifluidic devices.

Author affiliations: [a]Shaanxi Basic Discipline (Liquid Physics) Research Center, School of Physical Science and Technology, Northwestern Polytechnical University, Xi'an, Shaanxi 710129, China; [b]Materials Sciences Division, Lawrence Berkeley National Laboratory, Berkeley, CA 94720; [c]Polymer Science and Engineering Department, University of Massachusetts, Conte Center for Polymer Research, Amherst, MA 01003; [d]Beijing Advanced Innovation Center for Soft Matter Science and Engineering, Beijing University of Chemical Technology, Beijing 100029, China; and [e]Advanced Institute for Materials Research, Tohoku University, Sendai 980-8577, Japan

Author contributions: X.L. and X.P. designed research; X.L., X.P., H.J., M.D., H.L., Z.Y., and Y.X. performed research; X.L., X.P., and T.P.R. analyzed data; and X.L. and T.P.R. wrote the paper.

The authors declare no competing interest.

This article is a PNAS Direct Submission.

[1]To whom correspondence may be addressed. Email: lixiaoguang@nwpu.edu.cn or tom.p.russell@gmail.com.

This article contains supporting information online at https://www.pnas.org/lookup/suppl/doi:10.1073/pnas.2302907120/-/DCSupplemental.

Published July 3, 2023.

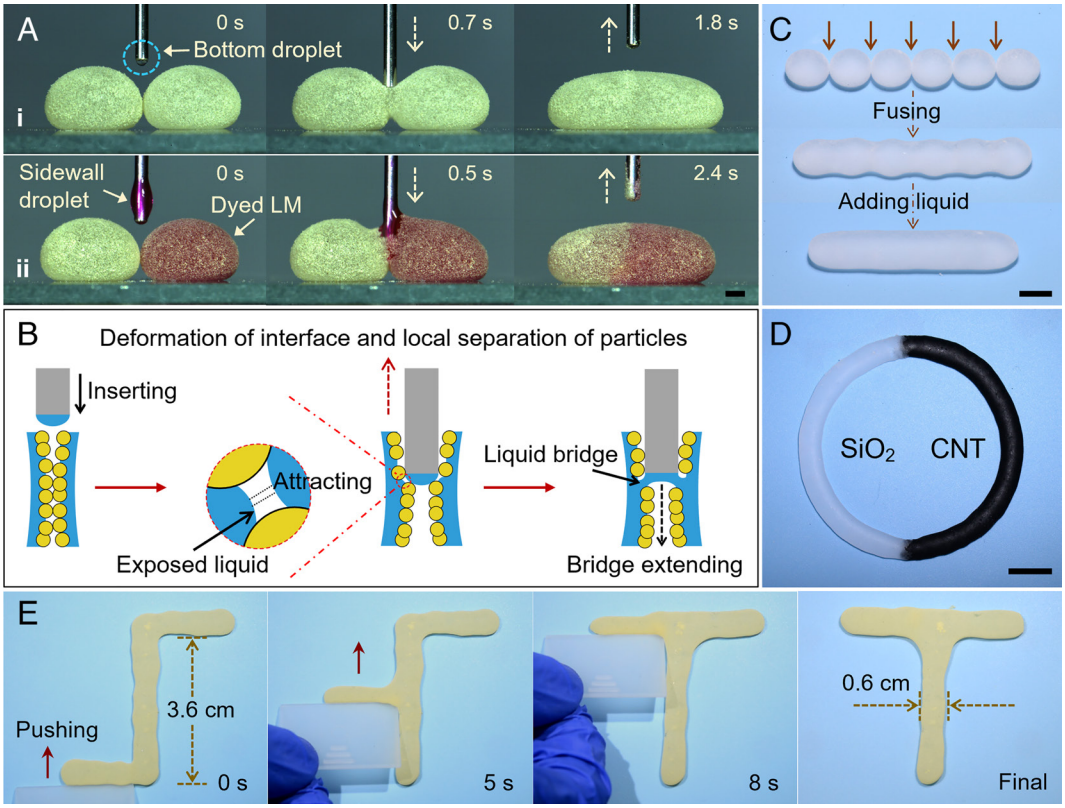

Fig. 1. Particle channel preparation and reconfiguration. (*A*) Fusion processes of 50 μL LMs, triggered by the *Bottom* (*i*) and side (*ii*) droplets, respectively. Dashed arrows, needle moving directions; particles, foveolate lycopodium of 32 μm; and bar, 1 mm. (*B*) Typical interface scenario during liquid-assisted LM fusion. (*C*) Illustration of channel production by fusing six 100 μL LMs. Solid arrows, positions of wetted needle insertion; particles, sheet-like polytetrafluoroethylene (PTFE) of 50 μm; and bar, 5 mm. (*D*) Ring-shaped channel consisting of 12-μm spherical SiO_2 (*Left half*) particles and 23-nm alkylated carbon nanotubes (CNTs, *Right half*); and bar, 1 cm. (*E*) Process for reconfiguring a particle channel with a plastic sheet.

Results

Spherical liquid marbles (LMs) were produced by the common method of rolling liquid (water is used for simplicity) droplets on a powder bed comprised of hydrophobic particles (23, 24). In this process, the particles automatically covered the droplet to reduce the interfacial energy of the liquid/air/solid system. The energy decrease, ΔE, corresponding to the attachment of a smooth spherical particle, is determined by $\Delta E = -\pi R^2\gamma(1+cos\theta)^2$, where R is the particle radius, γ the liquid surface tension, and θ is the contact angle between the liquid and the particle given by $cos\theta = (\gamma_P - \gamma_{L,P})/\gamma$, where γ_P is the surface energy of the particle, and $\gamma_{L,P}$ is the interfacial energy between the particle and liquid (25). For common powder particles of micron or nanometer size, this energy gain is much greater than thermal energy so that the particles adhere strongly to the droplet surface, forming a stable shell that contains the liquid.

The fusion of two LMs is inhibited by the stable particle shells (26), requiring the liquid to cross two particle barriers and an air gap. Extreme conditions, such as high-speed impact (27) or the application of a high voltage (22) have been needed to overcome this. In the method described here, a needle with a suspended liquid droplet of the same fluid as in the LMs was inserted between two closely placed LMs (Fig. 1*A*, *SI Appendix*, Fig. S1, and Movies S1 and S2). The liquid placed between the two LMs replaces air, removing any air gap, allowing the liquid to come in direct contact with the particles. This leaves a layer of particles separating the same liquid and, energetically, removing the particles, removes the interfacial energies between the particles and the liquid. Capillary forces draw the liquid placed between the LMs into the particle assemblies on both LMs, allowing contact, forming a bridge between the LMs (Fig. 1*B*) that, once formed, fuses the droplets. The system will attempt to minimize the interfacial area, driving the liquid to a spherical shape or, if the surface assemblies jam, locking-in a nonequilibrium shape.

We note that the liquid droplet on the needle is essential for the fusion. Without the droplet, the insertion of the needle alone has a high probability of causing the LMs to roll away. Even with large volume LM drops where rolling is difficult, the fusion probability under the presence of intermediary liquids is still much higher than otherwise (*SI Appendix*, Fig. S2 and Movie S3).

Depending on the volume of the inserted droplet relative to that of the LMs and on any mechanical deformation resulting from the droplet insertion process, the fusion will generally lead to a reduction of the total surface area, an increase in the areal density of the particles, and a jamming of the particles, locking-in the joined LMs into a new shape. These shapes could range from a dumbbells, two spherical droplets connected by a bridge, to a lozenge or rounded cylindrical shape, or to a single distorted spherical shape. This enables tailoring the liquid shape based on the fusion of the two LMs. Furthermore, using this liquid-assisted fusion strategy, a channel structure can be fabricated by successively joining multiple LMs. Due to its openness, the shape of channel can be further modified by, for example, adding liquid to the concave areas, flattening the shape (Fig. 1*C* and *SI Appendix*, Fig. S3). This fusion strategy can also be used to join channels encased by different types of particles (Fig. 1*D*), and successive joining is not limited by the particle composition, shape, or size (*SI Appendix*, Fig. S4, scanning electron microscopic images of particles), affording a universal means for particle channel production. We note that when different particles are used, since the particle jamming is subsequent to the fusion process, they do not form a uniform, mixed coating but the particles remain separate, as shown in Fig. 1*D*, similar to that seen with fused droplets encased by nanoparticle surfactants in liquid environment (28). The reconfigurability of the particle-encased channels is manifest in the example of a network pattern being changed by pushing a channel arm to move along the trunk without damaging the connection (Fig. 1*E*, *SI Appendix*, Fig. S5, and Movie S4).

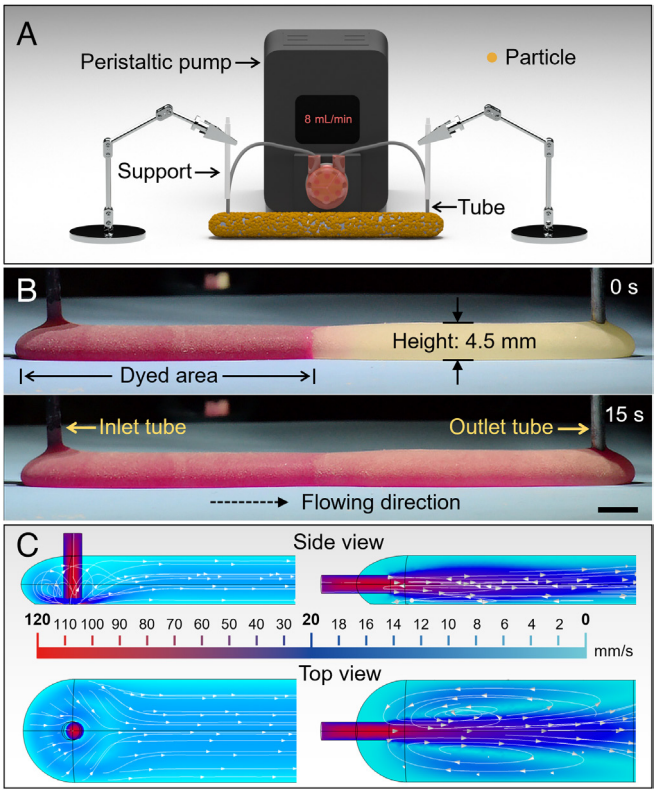

Fig. 2. Open millifluidics establishment and flow field adjustment. (*A*) Schematic of the setup for driving liquid to flow in a particle channel. (*B*) Photos of a particle channel made by joining a row of 300 μL LMs comprised of pure or dyed water, before and after pumping. Particles are lycopodium with a pumping rate of 8 mL/min, and a pressure of 46 Pa; and bar, 5 mm. Notably, the production of this ~7.7-cm channel took <1 min after the LMs were ready for use, owing to the simple fusion strategy. (*C*) Simulation patterns of flow fields in channel's *Left half*, under vertical and horizontal inlet tube insertions, respectively. Parameters in (*C*) identical with those in (*B*).

The external accessibility of the particle-encased constructs allows arbitrary insertion of flexible tubes connected to peristaltic or syringe pumps to direct liquid flow in the channels. For illustration, two tubes (tubes in this study all 1.8 mm diameter) of a peristaltic pump were inserted vertically into the ends of a particle channel (Fig. 2*A*). The pump generated a liquid flow that was easy to monitor with a dye in the liquid as it moved through the channel (Fig. 2*B*). The self-healing nature of the particle assemblies allowed the tube to be withdrawn and reinserted without leakage, enabling a simple means of adjusting the flow field. A vertical insertion led to a rapid formation of an exit-oriented flow field with a relatively uniform flow velocity, while horizontal insertion led to vortices and long-range gradual change in the flow velocity (Fig. 2*C* and *SI Appendix*, Fig. S6).

An important issue to address is the volume of liquid required to effectively manipulate the flow. The accessible volume of LMs usually ranges from several to hundreds of microliters. Thus, the width and height of the particle channel were on the millimeter scale. If the width is much larger than the tube diameter, homogenization could be retarded under a circular flow. A contrast experiment was performed using pure and dyed LMs with volumes ranging from 50 to 1,000 μL. The particle-encased channels made from the LMs had similar pure and dyed area lengths (Fig. 3*A*), with the LM-volume-determined width ranging from 5.8 to 17.1 mm. The channel height also increased with LM volume but by a much smaller amount, varying from 2.9 to 4.8 mm (Fig. 3*B*), where the 1,000 μL LM basically led to a maximum height achievable by an LM (29). Homogenization during the circular liquid flow was assessed colorimetrically (*SI Appendix*, Chart S1), with an index, I_{hom}, ranging from 0 to 1, where $I_{hom} = 1$ indicated complete homogenization (see the mathematical definition of I_{hom} in the *Materials and Methods* section). The results show that, although the large channel size led to a slow increase in I_{hom}, I_{hom} values for all the groups finally reached the same plateau (Fig. 3*C*), indicating that homogeneous distribution of material could be achieved over a large width range.

There were no upper limits on the lengths and widths of particle-encased channels produced by the joining strategy. In contrast, it was difficult to reduce the particle channel width to <1 mm. Smaller widths led to higher damage probability of the channels at high pumping rates. In a typical damage process, a particle channel with a right angle gradually expanded into a rugby-ball shape with the encased inner liquid being exposed (Fig. 3*D* and Movie S5), since the particle shell around the outlet tube tended to shrink with liquid extraction (Fig. 3*E*). Once the inserted tube was partly exposed to air during the shrinkage, air was sucked into the tube, causing the liquid removal rate to be less than the liquid insertion rate. As a result, the particle channel inflated, unjamming the particle assembly on the surface. The smaller the channel size, the greater is the likelihood of this occurring. For channels made up of 20 μL LMs, as illustrated in Fig. 3*D*, the safe operation in repetitive tests decreased from 100 to 20% when the pumping rate increased from 5 mL/min to 9 mL/min (*SI Appendix*, Fig. S7). In contrast, under the highest pumping rate we could achieve with our pump, 10 mL/min, the L-shaped channels that were made with LMs of ≥50 μL all ran safely without varying their shapes.

The advantages of the particle channels can be shown with three specific cases. In the first, a rod-shaped particle channel was connected to two peristaltic pumps, to realize a unidirectional flow (Fig. 4 *A*, *i*). A small volume of a dye solution was injected into the channel center (Fig. 4 *A*, *ii*), and the dye was driven to one end and out of the channel by flow (Fig. 4 *A*, *iii* and Movie S6). While a trivial example, this simple injection of the dye, could not be done in a closed channel configuration. In the second example, a Y-shaped particle channel was connected to two pumps, producing two closed circuits (Fig. 4 *B*, *i*). After homogenizing the dye distribution in each circuit, one of the circuits was severed (Fig. 4 *B*, *ii*). Subsequently, the two ends of the remaining channel were connected to one pump, producing a new closed circuit in which the two dyes were then mixed homogeneously (Fig. 4 *B*, *iii* and Movie S7). Such versatility in the redirection of the flow pattern is not possible with closed microfluidic devices and has great potential for material synthesis, information processing, and organic handling.

In the third example, a particle channel containing tumor cells (human osteosarcoma, 143B) was placed in an incubator for 24-h cell culture, generating large three-dimensional (3D) cell spheroids (Fig. 5*A*). These cell spheroids were shown to be healthy by further culturing them on a commonly used cell culture plate, in which the bottom cells grew by adhering to the substrate and, thus, spread gradually (Fig. 5*B* and *SI Appendix*, Fig. S8). In contrast to the culture in the particle channel, directly culturing the 143B cells on a plate resulted in two-dimensional (2D) patterns (Fig. 5*C*). The achievement of 3D culture was attributed to the nonwetting of the walls, preventing the wall-adhering cell growth route. The channel containing the cell spheroids was then grafted with another channel containing extracellular vesicles (EVs) by our liquid-assisted fusion means, followed by connection with one pump for mixing the cell spheroids and the EVs via circular flow (Fig. 5*D*). Finally, the mixture was incubated in the particle channel for 4 h and then extracted

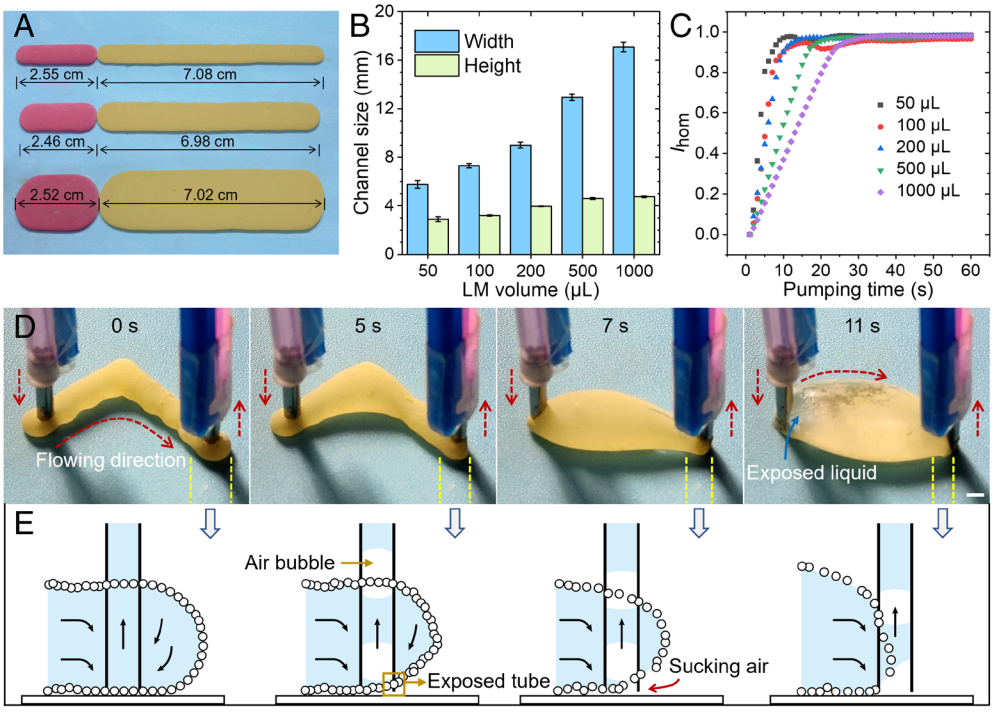

Fig. 3. Working efficiency and safety of open millifluidics. (*A*) Particle channel precursors obtained from fusing linearly arrayed lycopodium LMs of 50, 200, and 1,000 μL, respectively, from *Top* to *Bottom*, where pure and dyed parts were then subjected to fusion. (*B*) Channel's width and height vs. component LM's volume. (*C*) Homogenization index vs. the pumping time, under vertical tube insertion at channel ends and pumping rate of 8 mL/min. (*D*) Damage process of a particle channel, made up of 20 μL lycopodium LMs; under pumping rate of 7 mL/min; and bar, 2 mm. (*E*) Schematics depicting the scenario around outlet tube during damage.

by piercing the particle shell for test. The results showed that the cellular internalization of EVs was realized (Fig. 5*E* and *SI Appendix*, Fig. S9), establishing the foundation for EV-based cell regulation. The advantages here include 1) the natural ability of the particle channel in 3D cell culture, which is difficult to realize in solid containers; 2) the facile and time-saving process for sample mixing and extraction; and 3) the effective platform that allows routine biological interactions. The design of this case demonstration was inspired by the use of nonwetting droplets for 3D cell culture (30, 31) and applying EVs for cancer therapy (32). Further exploration of such designs with various tumors and EVs and in-depth biochemical analysis can undoubtedly lead to more attractive results. We expect many other biomedical applications using the particle channel-based millifluidic devices.

Notably, evaporation is inevitable through the porous particle shell and could be a concern in applications. For this, sealing the

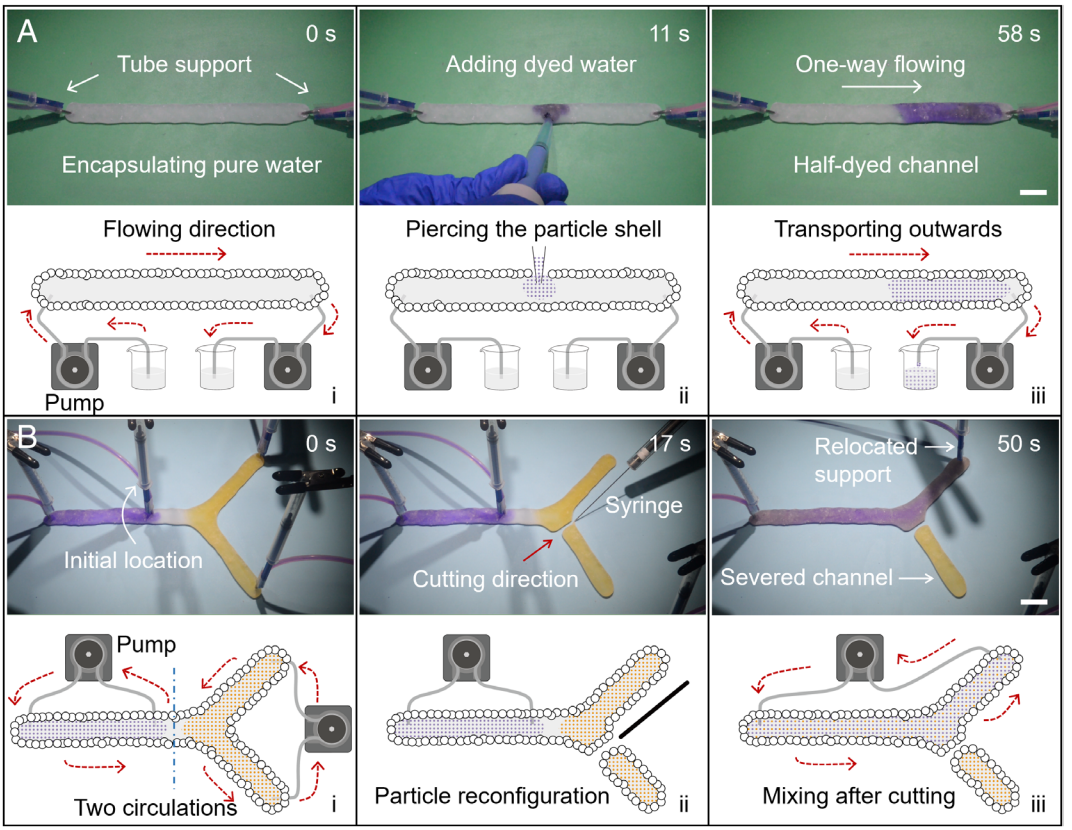

Fig. 4. Images and schematics illustrating typical manipulations that are especially applicable for open millifluidics. (*A*) Substance addition and transportation. Pumping rate, 4 mL/min. (*B*) Substance separation and mixing. Pumping rate, 8 mL/min; particle channels produced by 500 μL PTFE LMs; and bars, 2 cm.

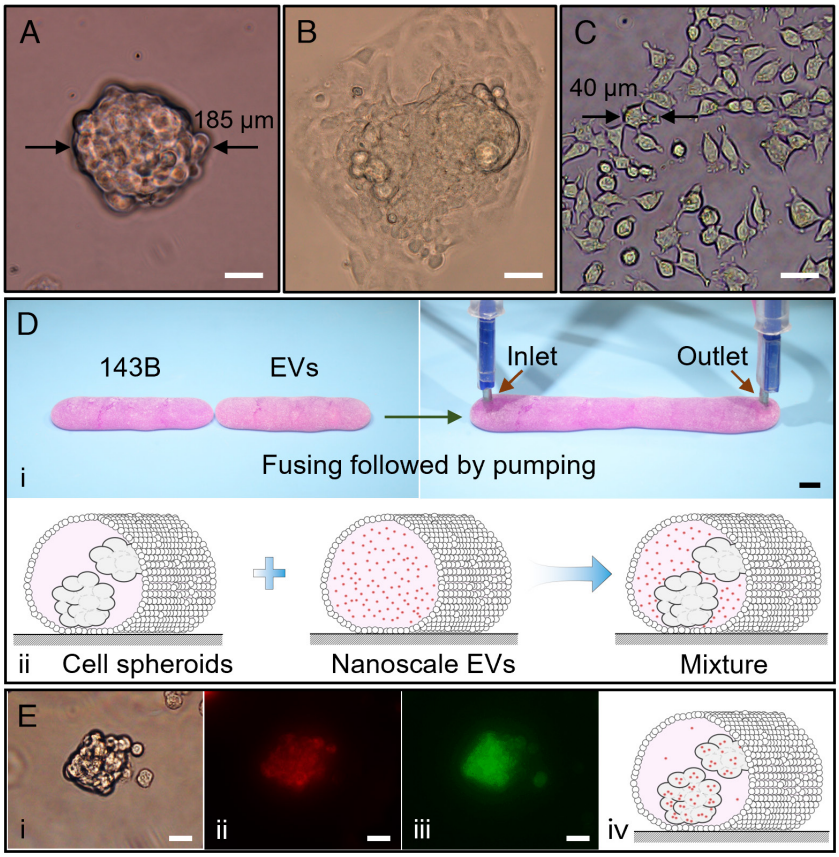

Fig. 5. 3D cell culture and cellular internalization using particle channels. 143B cells after 24-h culture in a particle channel (*A*) and then 12-h culture on a culture plate (*B*). (Bars, 50 μm.) (*C*) 143B cells after 24-h culture directly on a culture plate. (Bar, 50 μm.) (*D*) Individual and fused particle channels for mixing 143B cell spheroids and EVs (*i*) and the schematics depicting this process (*ii*). (Bar, 5 mm.) (*E*) Bright-field (*i*) and fluorescent (*ii* and *iii*) microscopic images of the 143B-EV mixture after 4-h incubation. Red and green staining (DiI and Calcein-AM) indicates the EVs and the 143B cells, respectively. The color overlap indicated by comparing panel *ii* and *iii* implies the cellular internalization of the EVs. Panel *iv* depicts the scenario of the internalization. (Bars, 50 μm.)

device, increasing the humidity, and replenishing liquid are all effective solutions.

Conclusions

In summary, we have realized open millifluidic devices with powder particle-encased channels for working in air environment, which can be produced by joining LMs by a controlled fusion process. Owing to the openness of the constructs, external devices, like peristaltic or syringe pumps, can be directly connected or disconnected from the particle channel at arbitrary locations. Liquids can be added or extracted at any location along the channel. These particle-encased constructs can be reconfigured, grafted, and segmented, without leakage of the inner liquid, due to the self-healing nature of the particle assemblies. Perhaps one of the more powerful aspects of the channel strategy here is the range of materials that can be used to encase the liquid, with a broad range of insensitivity to the particle size, shape, and composition.

Materials and Methods

Chemicals. Lycopodium, PTFE, alkylated SiO_2, and CNT powders were purchased from Aladdin Shanghai Biochemical Technology Co., Ltd. The CNT powder was treated by a chemical vapor deposition process, in which the powder was placed together with a plate of hexamethyldisilazane in a closed container at room temperature for 5 h. This process increased the methyl groups on the CNT particles, improving the hydrophobicity and thereby ensuring the formation of the CNT LMs as well as the CNT particle channel.

Liquid-Assisted LM Fusion. A wetted syringe needle adhered by a bottom or side droplet, as illustrated in Fig. 1*A*, was obtained simply by extruding a droplet from the needle or dipping the needle from a liquid pool. This process together with the following needle insertion between two LMs to trigger their fusion, either by using the apparatus or hand operation, takes only seconds. The substrates that supported the LMs or the particle channels need to be hydrophobic to ensure the safe operation. The effects of substrate material and surface roughness on the LM fusion are negligible. In this work, superhydrophobic SiO_2 films (33) were produced on glass slides and polypropylene sheets, with the coated substrates having root mean square surface roughnesses of ~5 and 125 nm, respectively.

Biological Processes. Human embryonic kidney 293T cells American Type Culture Collection (ATCC) were employed for generating EVs that were then labeled using DiI. 143B cells were cultured on plates before being used in the particle channels. In a plate, the cultured cells adhered to the substrate. They were then suspended in the Dulbecco's 223 modified Eagle's medium (Biological Industries) with 10% (v/v) Fetal Bovine Serum (FBS), by routine operation with trypsin added for cell detachment. Then, the cell suspension was used to make particle channels where the cells were cultured for 24 h, in a humidified atmosphere containing 5% CO_2/95% air at 37 °C, producing 3D cell spheroids. After mixing in the merged particle channel, the 143B cell spheroids and the DiI-labeled EVs were therein incubated for 4 h. Then the cells were rinsed three times with phosphate buffer saline (PBS) solution and labeled using Calcein-AM before the fluorescence microscopy test.

Characterizations. The fusion processes were monitored by a color high-speed camera (Fastcam Mini UX100, Photron Ltd. Tokyo, Japan). The size and shape of the powder particles were observed/measured by a scanning electron microscope (Verios G4, Field Electron and Ion Company, USA). The cells were observed using an inverted fluorescence microscope (IX73P2F, Olympus, Japan).

Simulation of the Flow Fields. The software Comsol Multiphysics was employed for the flow field simulation. The fluid flow module was adopted. The channel was built in the software with the size of 52×9×6.5 mm, corresponding to the real particle channel made up of eight 300 μL LMs. There is no option of particle channel in the software, while the experimental results indicate that the flow in a particle channel is basically identical to that in a common solid channel; therefore, continuous and dense PTFE, with hydrophobicity, was employed as the channel

material in the software for simulation. Stainless steel and water were chosen as the tube material and the flowing liquid, respectively. The slide velocities at the walls were set as 0 m/s.

Determination of the Homogenization Index. To quantitatively describe the degree of homogenization, an index, I_{hom}, was proposed in our colorimetric method. To obtain an I_{hom} value for a given pumping time, three particle channel photographs were necessary. The first was the beginning channel, i.e., channel corresponding to pumping time $t = 0$ s. The second was the channel undergone pumping for a given time, i.e., channel corresponding to t. The third was the particle channel undergone pumping for sufficient long time which resulted in perfect/complete homogenization. These three particle channel photographs were distinguished by color intensity distributions. They were imported into the software Matlab and transformed into grayscale images. Then, their pixel matrixes were created with each pixel characterized by a specific gray value. The three matrixes were then put into Eq. **1** for I_{hom} calculation, where subscripts *0*, *t*, and *perf* refer to the first, second, and the third particle channel, and *c* and *r* the column and row of a matrix, respectively. Eq. **1** is mainly based on matrix subtraction which reflects the difference in color intensity distribution between two particle channel images. The determination process of I_{hom} is summarized in *SI Appendix*, Chart S1.

$$I_{hom} = 1 - \sqrt{\frac{\frac{1}{c \times r}\sum_c \sum_r \left(M_t - M_{perf}\right). * \left(M_t - M_{perf}\right)}{\frac{1}{c \times r}\sum_c \sum_r \left(M_0 - M_{perf}\right). * \left(M_0 - M_{perf}\right)}}. \quad [\mathbf{1}]$$

Data, Materials, and Software Availability. There are no data underlying this work.

ACKNOWLEDGMENTS. This work was financially supported by the National Natural Science Foundation of China (Grant Nos. 11974280 and 51672224), and Projects of Interdisciplinary, NWPU (Grant No. 0202022GH0306). T.P.R. was supported by the U.S. Department of Energy, Office of Science, Office of Basic Energy Sciences, Materials Sciences and Engineering Division under Contract No. DE-AC02-05-CH11231 within the Adaptive Interfacial Assemblies Towards Structuring Liquids program (KCTR16).

1. W. S. Wang, S. A. Vanapalli, Millifluidics as a simple tool to optimize droplet networks: Case study on drop traffic in a bifurcated loop. *Biomicrofluidics* **8**, 064111 (2014).
2. L. Chen *et al.*, Millifluidics, microfluidics, and nanofluidics: Manipulating fluids at varying length scales. *Mater. Today Nano* **16**, 100136 (2021).
3. L. Wang, L. R. Karadaghi, R. L. Brutchey, N. Malmstadt, Self-optimizing parallel millifluidic reactor for scaling nanoparticle synthesis. *Chem. Commun.* **56**, 3745–3748 (2020).
4. V. Sans, L. Porwol, V. Dragone, L. Cronin, A self optimizing synthetic organic reactor system using real-time in-line NMR spectroscopy. *Chem. Sci.* **6**, 1258–1264 (2015).
5. C. Li *et al.*, Under oil open-channel microfluidics empowered by exclusive liquid repellency. *Sci. Adv.* **6**, eaay9919 (2020).
6. E. J. Walsh *et al.*, Microfluidics with fluid walls. *Nat. Commun.* **8**, 816 (2017).
7. P. Dunne *et al.*, Liquid flow and control without solid walls. *Nature* **581**, 58–62 (2020).
8. B. P. Casavant, E. Berthier, A. B. Theberge, D. J. Beebe, Suspended microfluidics. *Proc. Natl. Acad. Sci. U.S.A.* **110**, 10111–10116 (2013).
9. W. Feng *et al.*, Harnessing liquid-in-liquid printing and micropatterned substrates to fabricate 3-dimensional all-liquid fluidic devices. *Nat. Commun.* **10**, 1095 (2019).
10. M. Cui, T. Emrick, T. P. Russell, Stabilizing liquid drops in nonequilibrium shapes by the interfacial jamming of nanoparticles. *Science* **342**, 460–463 (2013).
11. X. Liu *et al.*, Reconfigurable ferromagnetic liquid droplets. *Science* **365**, 264–267 (2019).
12. A. B. Subramaniam, M. Abkarian, L. Mahadevan, H. A. Stone, Non-spherical bubbles. *Nature* **438**, 930 (2005).
13. S. M. Salehabad, S. Azizian, S. Fujii, Shape-designable liquid marbles stabilized by gel layer. *Langmuir* **35**, 8950–8960 (2019).
14. X. Li, J. Shen, Deforming water droplets with a superhydrophobic silica coating. *Chem. Commun.* **49**, 10016–10018 (2013).
15. X. Li *et al.*, Liquid plasticine: Controlled deformation and recovery of droplets with interfacial nanoparticle jamming. *Soft Matter* **12**, 1655–1662 (2016).
16. J. Niu *et al.*, Liquid plasticine integrated with isoelectric focusing for miniaturized protein analysis. *Anal. Chem.* **92**, 9048–9056 (2020).
17. X. Li, H. Shi, Y. Hu, Rod-shaped liquid plasticine for gas diffusion detection. *Soft Matter* **15**, 3085–3088 (2019).
18. X. Li *et al.*, Liquid shaping based on liquid pancakes. *Adv. Mater. Interfaces* **5**, 1701139 (2018).
19. X. Li, Liquid marbles and liquid plasticines with nanoparticle monolayers. *Adv. Colloid Interface Sci.* **271**, 101988 (2019).
20. X. Li, X. Pang, Liquid plasticines: Attributive characters, preparation strategies and application explorations. *Prog. Chem.* **34**, 1760–1771 (2022).
21. F. Geyer *et al.*, Polyhedral liquid marbles. *Adv. Funct. Mater.* **29**, 1808826 (2019).
22. Z. Liu *et al.*, Electrocontrolled liquid marbles for rapid miniaturized organic reactions. *Adv. Funct. Mater.* **29**, 1901101 (2019).
23. P. Aussillous, D. Quéré, Liquid marbles. *Nature* **411**, 924–927 (2001).
24. X. Pang *et al.*, Oscillation-induced mixing advances the functionality of liquid marble microreactors. *ACS Appl. Mater. Interfaces* **14**, 11999–12009 (2022).
25. P. Aussillous, D. Quéré, Properties of liquid marbles. *Proc. R. Soc. A.* **462**, 973–999 (2006).
26. E. Bormashenko, Liquid marbles, elastic nonstick droplets: From minireactors to self propulsion. *Langmuir* **33**, 663–669 (2017).
27. B. Wang *et al.*, On-demand coalescence and splitting of liquid marbles and their bioapplications. *Adv. Sci.* **6**, 1802033 (2019).
28. G. Xie *et al.*, Hanging droplets from liquid surfaces. *Proc. Natl. Acad. Sci. U.S.A.* **117**, 8360–8365 (2020).
29. R. Wang, X. Li, On the effective surface tension of powder-derived liquid marbles. *Powder Technol.* **367**, 608–615 (2020).
30. F. Sarvi *et al.*, Cardiogenesis of embryonic stem cells with liquid marble micro-bioreactor. *Adv. Healthcare Mater.* **4**, 77–86 (2015).
31. T. Arbatan *et al.*, Tumor inside a pearl drop. *Adv. Healthcare Mater.* **1**, 467–469 (2012).
32. X. Zhang *et al.*, Engineered extracellular vesicles for cancer therapy. *Adv. Mater.* **33**, 2005709 (2021).
33. X. Li, J. Shen, A facile two-step dipping process based on two silica systems for a superhydrophobic surface. *Chem. Commun.* **47**, 10761–10763 (2011).